The Astrophysical Journal, 947:59 (14pp), 2023 April 20 https://doi.org/10.3847/1538-4357/acc73b

Target-of-Opportunity Observation Detectability of Kilonovae with WFST

Zheng-Yan Liu[1,2], Zhe-Yu Lin[1,2], Ji-Ming Yu[3], Hui-Yu Wang[1,2], Gibran-Marc Mourani[1,2], Wen Zhao[1,2], and Zi-Gao Dai[1,2]

[1] CAS Key Laboratory for Researches in Galaxies and Cosmology, Department of Astronomy, University of Science and Technology of China, Chinese Academy of Sciences, Hefei, Anhui 230026, People's Republic of China; ustclzy@mail.ustc.edu.cn, wzhao7@ustc.edu.cn
[2] School of Astronomy and Space Sciences, University of Science and Technology of China, Hefei 230026, People's Republic of China
[3] Department of Astronomy, School of Physics and Astronomy, Shanghai Jiao Tong University, Shanghai 200240, People's Republic of China
Received 2022 November 1; revised 2023 March 22; accepted 2023 March 22; published 2023 April 21

Abstract

Kilonovae are approximately thermal transients, produced by the mergers of binary neutron stars (BNSs) and neutron star (NS)–black hole binaries. As the optical counterpart of the gravitational-wave event GW170817, AT2017gfo is the first kilonova detected with smoking-gun evidence. Its observation offers vital information for constraining the Hubble constant, the sources of cosmic *r*-process enrichment, and the equation of state of NSs. The 2.5 m Wide-Field Survey Telescope (WFST) operates in six bands (*u, g, r, i, z, w*), spanning from 320 to 925 nm. It will be completed in the first half of 2023, and with a field-of-view diameter of 3°, aims to detect kilonovae in the near future. In this article, considering the influence of the host galaxies and sky brightness, we generate simulated images to investigate WFST's ability to detect AT2017gfo-like kilonovae. Due to their spectra, host galaxies can significantly impact kilonova detection at longer wavelengths. When kilonovae are at peak luminosity, we find that WFST performs better in the *g* and *r* bands and can detect 90% (50%) of kilonovae at a luminosity distance of 248 Mpc (338 Mpc) with 30 s exposures. Furthermore, to reflect the actual efficiency under target-of-opportunity observations, we calculate the total time of follow up under various localization areas and distances. We find that if the localization areas of most BNS events detected during the fourth observing (O4) run of LIGO and Virgo are hundreds of deg^2, WFST is expected to find ∼30% of kilonovae in the first two nights following the detection of a GW event produced by a BNS during the O4 period.

Unified Astronomy Thesaurus concepts: Gravitational wave astronomy (675); Neutron stars (1108)

1. Introduction

Mergers of binary neutron stars (BNSs) and neutron star–black hole (NS–BH) binaries have been thought to generate the neutron-rich ejecta through rapid neutron capture (*r*-process) nucleosynthesis (Lattimer & Schramm 1974; Lattimer et al. 1977; Eichler et al. 1989). The expanding ejecta heated up by the radioactive decay of *r*-process nuclei can produce a type of transient whose luminosity is approximately a thousand times brighter than a typical nova theoretically, so named a "kilonova" (Li & Paczyński 1998; Metzger et al. 2010). In addition, it has been proposed that the merger of BNSs or NS–BH binaries can also produce short-duration gamma-ray bursts (sGRB; Paczynski 1986; Narayan et al. 1992; Popham et al. 1999), thus sGRB emission is expected to accompany a kilonova and a gravitational-wave (GW) burst if the jet is pointing toward Earth (Metzger & Berger 2012; Tanvir et al. 2013; Troja et al. 2019; Lamb et al. 2019; Jin et al. 2020).

On 2017 August 17 at 12:41:04.47 UTC, the first BNS merger GW source GW170817 was detected by the Advanced Laser Interferometer Gravitational-Wave Observatory (aLIGO) and Virgo with a false-alarm-rate estimate of less than one per 8.0×10^4 yr (Abbott et al. 2017). After the GW detection alert was triggered (∼1.7 s), the Fermi Gamma-Ray Space Telescope and the International Gamma-Ray Astrophysics Laboratory (INTEGRAL) detected the sGRB 170817A, which lasted about 2 s (Goldstein et al. 2017; Savchenko et al. 2017). Based on the sky map constrained by the GW and sGRB signals, telescopes all around the world started to search for the optical counterpart of GW170817. The Swope team was the first to observe the candidate, declaring it to be located in NGC 4993, which was subsequently confirmed to be a kilonova by other telescopes' observations, and named as AT2017gfo. (e.g., Coulter et al. 2017; Cowperthwaite et al. 2017; Evans et al. 2017; Kasliwal et al. 2017; Pian et al. 2017; Shappee et al. 2017; Smartt et al. 2017; Tanvir et al. 2017).

A telescope with a large field of view (FoV) is necessary for searching for the electromagnetic counterpart of such mergers, due to the large localization area with 10^1–10^3 deg^2 from GW detectors. The 2.5 m Wide-Field Survey Telescope (WFST) will be installed at the summit of the Saishiteng Mountain near Lenghu, which is planned to be completed in the first half of 2023, and commence operations subsequently. With a FoV of 6.55 deg^2, WFST will scan the Northern sky in six optical bands (*u, g, r, i, z, w*) reaching a depth of 22.40, 23.35, 22.95, 22.59, 21.64, and 22.96 AB mag in a nominal 30 s exposure in the optical bands, respectively, which meets the scientific requirements for kilonova detection. There is a median seeing of 0.″75 (Deng et al. 2021) in the Lenghu site, which provides an ideal environment for WFST. Given these parameters and its geographical location, WFST can bridge the longitudinal gap between other wide-field instruments and has the potential to be one of the major GW follow-up instruments in the Northern Hemisphere for the upcoming fourth (O4) and fifth observing (O5) run of ground-based GW detectors.

In the third observing (O3) run of LIGO and Virgo, in order to search for new kilonovae, many instruments including the Zwicky Transient Facility (ZTF; Bellm et al. 2019; Graham

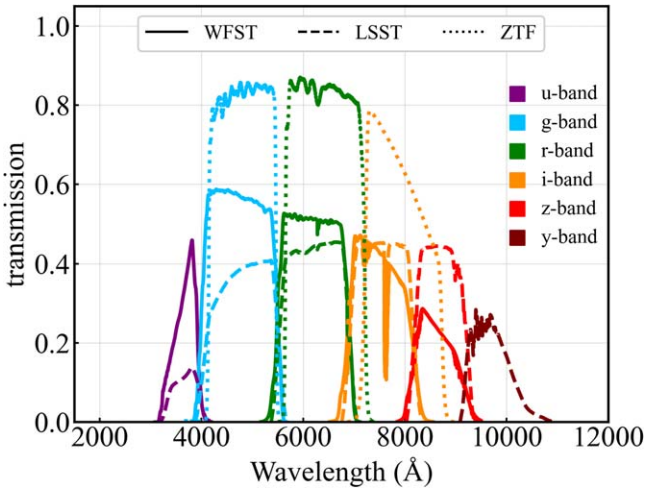

Figure 1. The transmission curves of the telescope systems of WFST, ZTF, and LSST.

et al. 2019) and the Dark Energy Camera (DECam; Flaugher et al. 2015) have made extensive follow-up observations. However, there was no conclusive evidence for kilonovae detection by the end of the O3 run. (Andreoni et al. 2019; Ackley et al. 2020; Andreoni et al. 2020; Kasliwal et al. 2020; Anand et al. 2021; Tucker et al. 2022). To improve follow-up observations with WFST in upcoming O4 and O5, we need to handle the trade-off between exposure time and sky coverage, using previous observations for reference. Recently, some studies on kilonova detectability predicted the expected number of kilonovae for various wide-field instruments (Cowperthwaite & Berger 2015; Scolnic et al. 2017; Cowperthwaite et al. 2019; Zhu et al. 2023; Chase et al. 2022; Wang et al. 2022). Based on the different observation cadences, Cowperthwaite et al. (2019) explored the efficiency of searching for kilonovae randomly with the Large Synoptic Survey Telescope (LSST; LSST Science Collaboration et al. 2017; Ivezić et al. 2019) at the Vera C. Rubin Observatory. Their research concluded that it is more effective to search for kilonovae after a GW trigger than via serendipitous observations. By considering the afterglows of sGRBs and the viewing angle, for AT2017gfo-like kilonovae, Zhu et al. (2023) studied the prospect of finding different combinations of kilonovae and GRB afterglows. Chase et al. (2022) calculated the detection depth of thirteen wide-field instruments based on a specific kilonova model and a grid of parameters. In these works, the influence of image subtraction and the host galaxy on kilonova detection is always ignored, therefore the detection depth will be overestimated, resulting in more kilonovae predicted to be found. In practice, evaluating these effects is also needed to select the appropriate exposure time in target-of-opportunity (ToO) observations.

In this work, we assess the ability of WFST to detect AT2017gfo-like kilonovae with mock observations. We focus on five of WFST's optical band filters, excluding the *w* band, which is a broad bandpass and is not helpful to measure color information of kilonovae (the transmission of other bands is shown in Figure 1). By considering galaxies in a synthetic galaxy catalog as hosts of kilonovae, we investigate and quantify the influence of image subtraction and the host galaxy on kilonova searches. The method of mock observation and its verification and accuracy are described in Section 2. In Section 3, the details about adding a host galaxy into an image are introduced, and we display and discuss the simulation results of kilonova detectability for WFST, LSST, and ZTF. In Section 4, we optimize the exposure time selection upon these results and explore the follow-up capacity of WFST by estimating the average total time spent in a ToO observation. Finally, as a complement to the case of AT2017gfo-like kilonovae, we discuss the detection ability for other kilonovae and summarize our results in Section 5. Throughout this study, we adopt a standard Λ-cold dark matter (ΛCDM) cosmology with parameters $H_0 = 69.3\ \mathrm{km\ s^{-1}\ Mpc^{-1}}$, $\Omega_M = 0.287$, and $\Omega_\Lambda = 0.713$ (Hinshaw et al. 2013).

2. Simulation Process

In this section, we introduce the method of simulated image synthesis and test it by computing the kilonova detection depth of WFST with a flat background. The main steps of the synthesis process are as follows.

Kilonova template: the luminosity evolution of AT2017gfo can be explained and fitted by many kilonova models (e.g., Kasen et al. 2017; Villar et al. 2017; Yu et al. 2018; Bulla 2019; Hotokezaka & Nakar 2020; Wollaeger et al. 2021). The main differences between these models are the mechanism that powers the early emission, the ejecta matter composition and morphology, and the calculation of radiation transfer. Given that there are few observations of kilonova except AT2017gfo, these models cannot be distinguished based on the limited observation data. The chance of detecting a kilonova depends on the template, which can be chosen from data or be generated by a theoretical model. Considering the lack of constraints on kilonova models and the uncertainties of the model parameters, we choose AT2017gfo as a source of reference in this study and obtain its lightcurve by `MOSFiT`.[4] Using AT2017gfo as the kilonova template leaves out the potential for kilonova diversity, which can affect the overall estimation of kilonova detection. Combined with a certain kilonova model, this influence is discussed specifically in Section 5.1.

`MOSFiT` is a python package that collects transient templates (e.g., kilonova, tidal disruption event (TDE), and supernova (SN)), which can be used to fit observations and generate theoretical light curves (Guillochon et al. 2018). The kilonova template in `MOSFiT` originates from Villar et al. (2017) where the authors constructed a spherically symmetric ejecta model composed of two or three components of matter. We choose the three-component model where these components have different opacities (κ) fixed in the model, which are named as blue ($\kappa = 0.5\ \mathrm{cm^2\ g^{-1}}$), purple ($\kappa = 3\ \mathrm{cm^2\ g^{-1}}$), and red ($\kappa = 10\ \mathrm{cm^2\ g^{-1}}$) components. There are three more free parameters to describe each component: mass ($M_{\rm ej}$), velocity ($v_{\rm ej}$), and temperature floor (T_c). In addition, the authors introduced a variance parameter (σ) in the likelihood function, which encompasses additional uncertainties in the model and/or data. To generate the lightcurves, the parameters of best-fit result in Villar et al. (2017) are adopted: $M_{\rm ej}^{\rm blue} = 0.020\ M_\odot$, $v_{\rm ej}^{\rm blue} = 0.266\ c$, $T^{\rm blue} = 674$ K, $M_{\rm ej}^{\rm purple} = 0.047\ M_\odot$, $v_{\rm ej}^{\rm purple} = 0.152\ c$, $T^{\rm purple} = 1308$ K, $M_{\rm ej}^{\rm red} = 0.011\ M_\odot$, $v_{\rm ej}^{\rm red} = 0.137\ c$, $T^{\rm red} = 3745$ K, and $\sigma = 0.242$. It is worth noting that the lightcurve fitting generated by different kilonova models can be somewhat different (Arcavi 2018). Especially

[4] https://github.com/guillochon/mosfit

Table 1
The Parameters and Information of the Telescopes Used in the Simulations for WFST, ZTF, and LSST

Telescope	Limiting Magnitude and Sky Brightness (mag & mag/arcsec^2)						Diameter (m)	Read-out Noise (e/pixel)	Pixel Scale (arcsec)	Image Quality (arcsec)	FoV (deg^2)	Ref
WFST	*u*	*g*	*r*	*i*	*z*	*w*	2.5	10	0.33	1.0	6.55	(1)
	22.40	23.35	22.95	22.59	21.64	22.96						
	22.29	22.12	21.58	21.29	20.29	...						
LSST	*u*	*g*	*r*	*i*	*z*	*y*	8.4	18	0.2	0.80	9.6	(2)
	23.87	24.82	24.36	23.93	23.36	22.47						
	22.96	22.26	21.20	20.48	19.60	18.61						
ZTF	*g*		*r*		*i*		1.2	8	1.0	2.0	47	(3)
	21.1		20.9		20.2							
	21.8		20.7		19.9							

Note. For each telescope, the upper and bottom rows are the 5σ limiting magnitude for a 30 s exposure and dark night-sky brightness, respectively. For the sky brightness of ZTF, we use the measurement of P200 to represent the sky background of the Palomar Observatory. References: (1) Lin et al. (2022) and Lei et al. (2023); (2) Ivezić et al. (2019) and Ivezić et al. (2010); and (3) Bellm et al. (2019) and P200 (2007).

for early-time ($\delta t < 10$ hr) kilonova emission, the lightcurve mainly depends on the model used due to a lack of observational data (Arcavi et al. 2017).

Image generation: we generate the simulated images by `GalSim`,[5] which is an open-source project providing a software library for simulating images of astronomical objects such as stars and galaxies in a variety of ways (Rowe et al. 2015). Taking into account the generation speed and computing resources, we produce simulated images with at least 200×200 pixels and place the target in the center. When a kilonova and its background are added into images, using point-spread functions (PSFs) integrated into `GalSim`, we consider the extension of the point source caused by the optical system and atmospheric seeing. In addition, Poisson noise and read-out noise can also be added to images by the built-in noise generators. The image quality and read-out noise we use in the simulation are shown in Table 1.

Photometry and evaluation criteria: by subtracting simulated reference images from science images, we can obtain difference images and perform photometry with `PythonPhot`[6] to judge whether the kilonova can be detected or not. `PythonPhot` is a python package translated from the DAOPHOT-type photometry procedures of the IDL AstroLib photometry algorithms (Landsman 1993; Jones et al. 2015). When a kilonova is relatively faint compared to its background, the measurement errors of the PSF-fitting photometry tool `PythonPhot` may be overestimated. So we use aperture photometry to assist the PSF-fitting photometry to get the signal-to-noise ratio (S/N) of the source. The diameter of the aperture is taken as 1.5 times the FWHM in each band. The FWHM of each band is computed based on the image quality parameters listed in Table 1. Among all the results presented in this article, we set the threshold of S/N = 5 to judge whether kilonovae can be detected or not.

To test and verify the ability of the simulation process, we consider a simple case where we insert kilonovae into the images' centers and choose a uniform background of sky brightness to compute its influence on detection. For kilonovae at different distances, we set a range of sky brightnesses to obtain the critical value at which the telescope can detect a kilonova. The relationship between luminosity distance and critical sky brightness in each bandpass of the 30 and 300 s exposures is shown in Figure 2. In this simulation, for each band we choose the peak luminosity of the kilonova as well as another two cases: one and two magnitudes fainter than the peak. The comparison of these results can reflect the change of detection depth as the kilonova evolves. From the observation of AT2017gfo, its magnitude faded at ~1 mag per day in the *g* and *r* bands (Kasliwal et al. 2020), thus the other two cases (one and two magnitudes fainter than the peak) roughly correspond the 2nd and 3rd day after a BNS merger. We find that the *g*, *r*, and *i* bands are better choices for WFST to search for kilonovae because of their deeper detection depths for a given exposure time.

According to the observation conditions of the Lenghu site reported in Deng et al. (2021), measured in the bandpass from 400 to 600 nm, during a fully clear new Moon phase, the night-sky brightness is 22.3 mag arcsec^{-2} in *V* band at most. The average night-sky brightness is around 22.0 mag arcsec^{-2} when the Moon is below the horizon. Considering a background mostly due to night-sky brightness, which corresponds to the case where the flux from a faint host galaxy can be ignored, we compute the detection depth of WFST. Each band brightness used is shown in Table 1. The detection depths of different situations are shown in Table 2. Due to the low transmission shown in Figure 1 or the effects of higher sky brightness, the detection ranges of the *u* and *z* bands are relatively low, thus they are not suitable for early searches for kilonovae. To verify the reliability of the result, we calculate the detection depth by comparing the kilonova magnitudes and the limiting magnitudes of WFST. Using the limiting magnitudes in Table 1, with 30 s exposures, the *g* and *i* bands have detection depths of 458 and 419 Mpc, respectively, at peak luminosity. The detection depths in Table 2 are shallower than those estimated simply using the limiting magnitude for the reason that in a more realistic situation, there will be contribution from noise introduced by image subtraction. Therefore, calculating the detection depth with only limiting magnitude can overestimate the detection rate of kilonovae.

3. The Influence from the Host Galaxy

Based on the image simulation process introduced in Section 2, in this section, we insert a host galaxy into the

[5] https://github.com/GalSim-developers/GalSim
[6] https://github.com/djones1040/PythonPhot

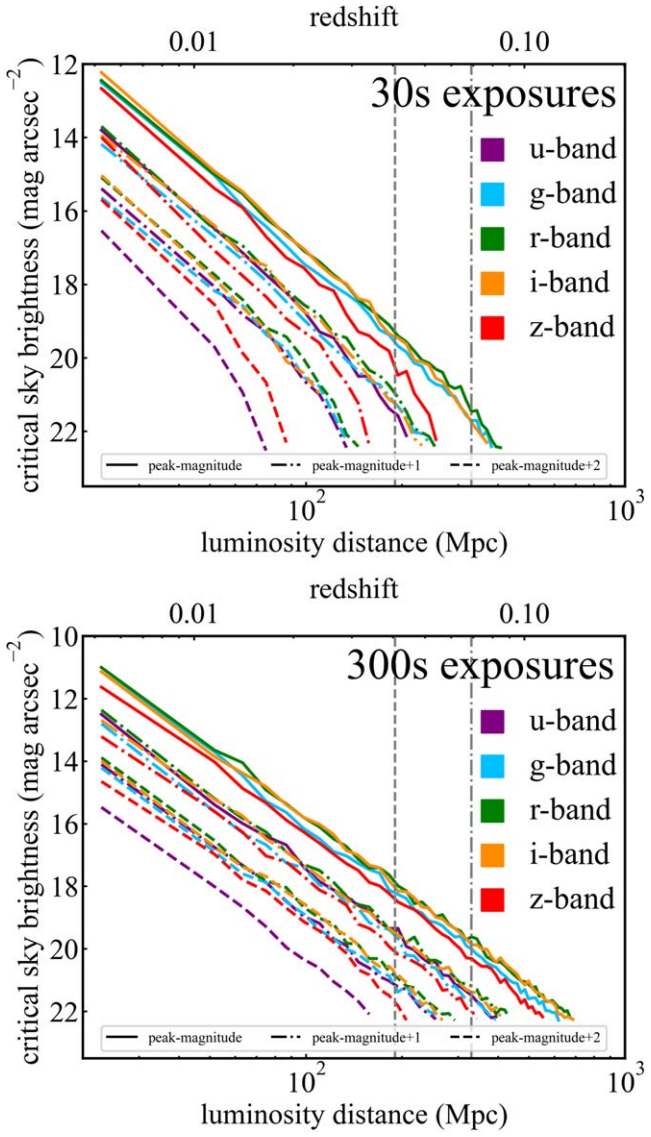

Figure 2. At different times of evolution of an AT2017gfo-like kilonova, the relationship between luminosity distance and critical sky brightness from image simulation with 30 and 300 s exposures. The gray dashed and dotted–dashed lines represent the detection range for a BNS occurring during O4 and O5, respectively (Abbott et al. 2020).

Table 2
The Detection Depths at Different Times of Evolution of an AT2017gfo-like Kilonova for WFST

Exposure (s)	Luminosity	Detection Depth (Mpc)				
		u	*g*	*r*	*i*	*z*
30	peak	210	357	338	302	202
	peak+1 mag	131	233	209	193	123
	peak+2 mag	73	131	127	112	69
300	peak	395	609	562	515	320
	peak+1 mag	257	375	366	317	206
	peak+2 mag	163	256	234	214	137

simulated image to consider its influence on the detection of the kilonova.

3.1. Galaxy Catalog and Building Sample

In order to take the host galaxy into account, a specific galaxy catalog needs to be input into the process of image synthesis. For optimizing the follow-up observations of GW alerts of compact binary mergers, some works have assembled known galaxy catalogs into larger, homogenized collections (White et al. 2011; Dálya et al. 2018, 2022). Using the observed galaxy catalogs can be more instructive and meaningful in making a follow-up strategy. However, the observed galaxy catalogs are always incomplete at large distances, and these catalogs do not always have enough information to insert galaxies into simulated images because of the lack of morphological descriptions. So we choose the synthetic galaxy catalog cosmoDC2[7] to consider the influence of the host galaxy.

CosmoDC2 is a large synthetic galaxy catalog which is made for dark energy science with LSST, based on a trillion-particle $(4.255\ \mathrm{Gpc})^3$ box cosmological *N*-body simulation (Korytov et al. 2019). CosmoDC2 covers 440 deg^2 sky area to a redshift $z = 3$, and there are many parameters in this catalog to describe and quantify the properties of each galaxy, such as stellar mass, morphology, and spectral energy distribution. These parameters can match well with the interfaces and functions of `GalSim`. Unlike the observed galaxy catalogs, we can easily add galaxies into images as we know their size and morphology. Nevertheless, bias from the actual case may exist. To make sure that the galaxies in the catalog can be consistent with a real situation, some comparisons including redshift distribution and color distribution have been done and shown in Korytov et al. (2019). Hence, choosing galaxies from CosmoDC2 in simulation should fairly reflect the influence of host galaxies of the real universe.

As we wish to consider the hosts of detectable kilonovae, some selections and filters are needed to build the simulated galaxy sample. According to the sensitivity of GW detectors for a BNS system of $1.4\,M_\odot + 1.4\,M_\odot$ in O4 and O5 (Abbott et al. 2020), the typical ranges of detected BNSs can reach 190 and 330 Mpc, which correspond to redshifts $z = 0.043$ and 0.072, respectively. Given the luminosity of kilonovae, we select galaxies with $z < 0.2$ in CosmoDC2 to simulate. Combined with some mechanisms of compact binary formation and the method of population synthesis, the properties of host galaxies of merging compact objects can be explored. Several works have attempted to study their properties with this approach (O'Shaughnessy et al. 2017; Cao et al. 2018; Giacobbo & Mapelli 2018; Lamberts et al. 2018; Mapelli et al. 2018; Artale et al. 2019; Toffano et al. 2019; Artale et al. 2020). These works have found that the merger rate of compact binaries depends on stellar mass, metallicity, and galaxy host type. Considering that the strongest correlation is between the merger rate and the stellar mass of the host galaxy relative to other parameters (Artale et al. 2019, 2020), to assign a weight to each galaxy, we adopt the 1D relationship of $z = 0.1$ of the fitting results between stellar mass (M_*) and BNS merger rate (n_{BNS}) according to Artale et al. (2020):

$$\log_{10}(n_{\mathrm{BNS}}/\mathrm{Gyr}) = (1.038 \pm 0.001)\log_{10}(M_*/M_\odot) - (6.090 \pm 0.010). \quad (1)$$

[7] https://github.com/LSSTDESC/cosmodc2

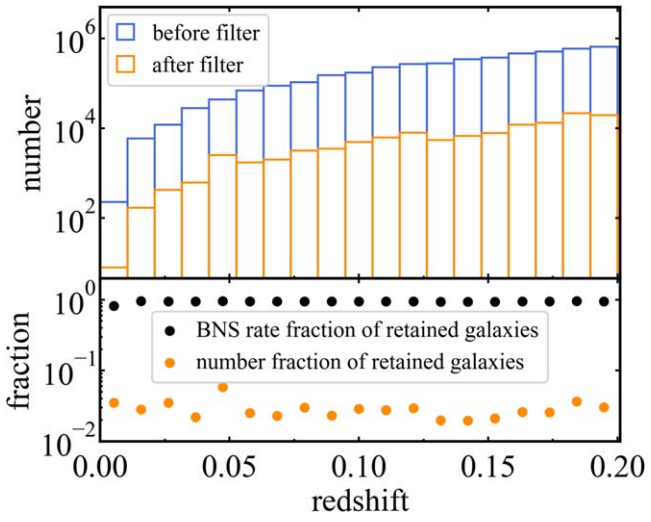

Figure 3. At each redshift, the number of galaxies before and after applying the filters and the fraction of the size and BNS merger rate of galaxy sample.

Comparing the fitting results between $z = 0.1$ and $z = 1$ in Artale et al. (2020):

$$\log_{10}(n_{\rm BNS}/{\rm Gyr}) = (1.109 \pm 0.001)\log_{10}(M_*/M_\odot) - (6.214 \pm 0.006), \quad (2)$$

the fitting factors in these two cases are not much different, therefore Equation (1) can be used under the redshift range of $z \leqslant 0.2$ in our simulation. We calculate the merger rates of galaxies that satisfy $M_* > 10^7\,M_\odot$. Since the size of the galaxy sample with $z < 0.2$ and $M_* > 10^7\,M_\odot$ is also too large, we further narrow down the sample by retaining only those objects with $\log_{10}(n_{\rm BNS}/{\rm Gyr}) > 4$, which roughly correspond to $M_* > 10^{10}\,M_\odot$. After filtering and dividing the galaxies into a series of subsamples with different redshifts, the number of galaxies and the BNS merger rate are shown in Figure 3. With the filter of $\log_{10}(n_{\rm BNS}/{\rm Gyr}) > 4$, for each galaxy subsample the size is greatly reduced, while the total BNS merger rate changes slightly, which means that most galaxies that contribute little to the merger rate are excluded.

3.2. Kilonova Offset to Galaxy Center

Adding a host galaxy into an image means considering an uneven background with a specific profile, therefore the relative location of the merger to its host is essential to investigate the influence of the host galaxy. There are two ways to explore the offset between the compact binary merger and the galaxy's center: the first is the population synthesis method, and the other is tracing the BNS merger by sGRB.

By population synthesis, it is found that most BNS mergers are far from the galaxy center, and the offset distribution depends on the gravitational potential, the metallicity of different galaxy types, and some parameters of compact binary including formation channel, initial location, kick velocity, and delay time (Bloom et al. 1999; Belczynski et al. 2002; Voss & Tauris 2003; Belczynski et al. 2006; Mapelli & Giacobbo 2018; Wang et al. 2020). By an observational and systematic analysis of the host galaxy, Fong et al. (2010, 2015) and Fong & Berger (2013) collected the host galaxy properties of 22 sGRBs and compared their projected offsets (both physical and normalized) with long GRBs, core-collapse SNe, and even Type Ia SNe. They found that most sGRBs are far from the galaxy center, which is consistent with the model where sGRBs originate from a compact binary merger. In addition, the multimessenger observations of GW170817 further confirmed the relationship between sGRBs and the merger of BNSs (Goldstein et al. 2017).

We choose to use sGRBs to trace the locations of BNS mergers and impose kilonovae into the images according to the projected offset distribution of sGRBs, which means that we assume sGRBs mostly originate from BNS mergers. Besides the 22 sGRBs reported in Fong et al. (2010) and Fong & Berger (2013), we collect five other sGRBs with reliable offset measurements from 2013 to 2020 and add them into sGRB sample, which can be seen in Table 3. The difference between the two samples is shown in Figure 4, where the projected physical offsets of the additional five sGRBs are consistent with the distributions of the previous works, and the offset median is 5.1 kpc compared to 4.5 kpc in Fong & Berger (2013). To obtain projected offsets between kilonovae and galaxy centers, we fit this sample of 27 sGRBs with a log-normal distribution using `statsmodels` (Seabold & Perktold 2010) based on the maximum likelihood method and the fitting result is:

$${\rm PDF}_{\rm fit}(r) = \frac{1}{(r - r_0)\sigma\sqrt{2\pi}}\exp\left(-\frac{(\ln(r - r_0) - \mu)^2}{2\sigma^2}\right), \quad (3)$$

where $\rm PDF_{fit}$ is the probability density function, r is in kpc, $r_0 = 0.24 \pm 0.23$, $\sigma = 1.26 \pm 0.23$, and $\mu = 1.44 \pm 0.27$. Using

Table 3
The Information of Additional Measurements of the Projected Offset from five sGRBs

sGRB	Redshift	Instrument	Filter	Offset ($''$)	Offset (kpc)	Offset (r_e)	Reference
150101B	0.1343	ACS	F606W	3.07 ± 0.03	7.35 ± 0.07	0.77 ± 0.03	Fong et al. (2016)
		WFC3	F160W	3.07 ± 0.03	7.35 ± 0.07	1.01 ± 0.03	
160821B	0.162	ACS	F606W	5.7	16.40 ± 0.12	⋯	Troja et al. (2019)
170817A	0.0973	ACS	F475W, F625W, F775W	10.315 ± 0.007	2.125 ± 0.001	0.64 ± 0.03[a]	Blanchard et al. (2017)
		WFC3	F110W, F160W	10.317 ± 0.005	2.125 ± 0.001	0.57 ± 0.05[a]	
181123B	1.754	Gemini-N	i	0.59 ± 0.16	5.08 ± 1.38	⋯	Paterson et al. (2020)
200522A	0.5536	WFC3	F125W	0.155 ± 0.054	1.01 ± 0.35	0.24 ± 0.04	Fong et al. (2021)
		WFC3	F160W	0.143 ± 0.029	0.93 ± 0.19	0.24 ± 0.04	

Note. The offsets are described in three ways, which are the angular distance in image, projected distance in kpc, and normalized distance by effective radius of galaxy.
[a] The half-light radius is obtained by the averages of the values from the optical and NIR Hubble Space Telescope observations in several filters.

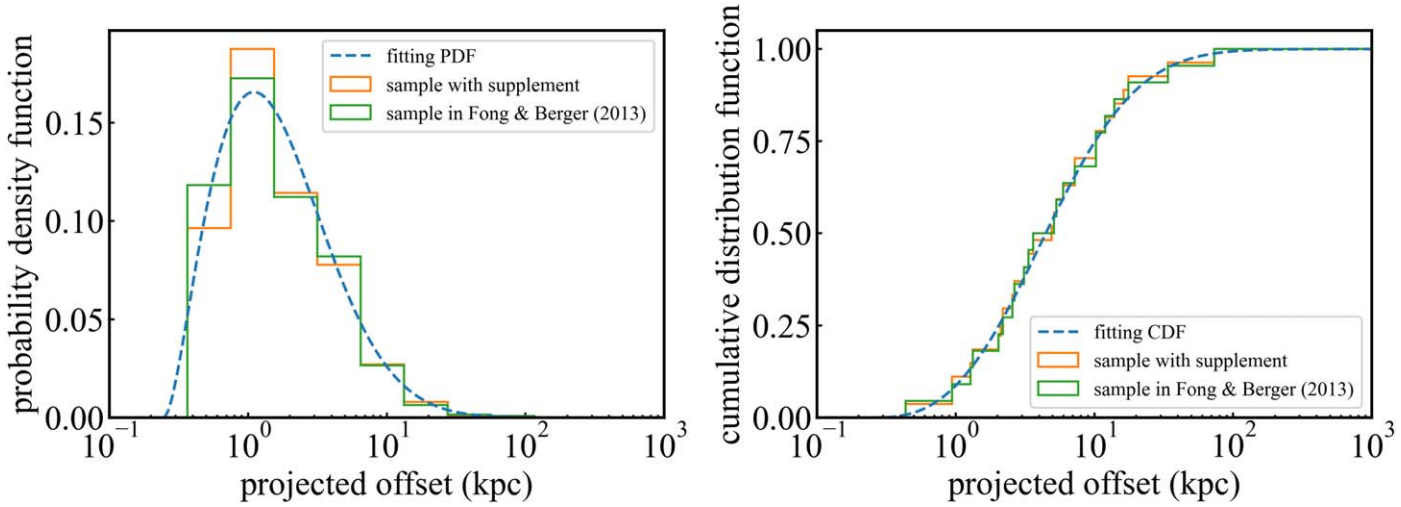

Figure 4. The probability density and cumulative distributions of the projected offset between the locations of sGRB and the centers of the host galaxies for the different samples and their fitting result.

the PDF in Equation (3), the projected offset between the BNS merger's location and the galaxy center can be obtained. Regarding the angular distribution of the merger, we assume a uniform distribution to sample the angle relative to the main axis of the galaxy in our simulation.

3.3. Results

We divide the redshift range of 0–0.2 in a grid of 75 bins and generate simulated images for galaxies in each bin. If the number of galaxies in a bin is more than 1000, we will randomly choose 1000 galaxies as the simulation sample to reduce the computing time appropriately. An example of simulated images with the host galaxy is presented in Figure 5. When a BNS merger is close to the galaxy's center, like Panel 5(b), the background is dominated by host luminosity. Otherwise, in Panel 5(a), the sky brightness will be vital for detection, and the sky brightness of each band in the simulation is shown in Table 1. According to the simulation process described in Sections 2 and 3, we generate simulated images for each galaxy in the different bands and judge whether kilonovae can be detected or not. By averaging these detection results, the weighted fraction of kilonovae that are detectable can be calculated combined with the BNS merger rate derived from Equation (1). The weighted fraction at different redshifts is called the detection efficiency in our following results. When an AT2017gfo-like kilonova is at peak luminosity, the results of the detection efficiency for WFST with the 30 and 300 s exposures are shown in Figure 6. When a BNS is at small luminosity distances, WFST can easily detect its kilonova emission, as was in the case of GW170817. As the luminosity distance increases, the detection efficiency decreases gradually. The speed of decrease is different for each band, which can reflect the influence of the host galaxy on detection combined with Figure 7. With the subsample at the redshift of $z = 0.114$ as an example, Figure 7 displays the flux distribution of galaxies of CosmoDC2 in the different bands of WFST. According to Figure 7, the longer wavelength of the band, the greater the mean and standard deviation of the flux distribution. In the u band, there is not much difference in the effect of kilonova detection between different galaxies, because their flux is more concentrated. As a result, the detection efficiency with the u band falls faster than the others. In contrast, the efficiency begins to decline earlier and declines more slowly in longer-wavelength bands. The detection depths with 90% and 50% efficiency are shown in Table 4. Compared with the case of the flat sky brightness in Table 2, the detection depth of 90% efficiency is reduced by 50–200 Mpc.

Cowperthwaite et al. (2019) found that searching for kilonovae serendipitously with a certain survey is not effective due to its low efficiency if the sensitivity and FoV of the telescope are insufficient. Host galaxies can further affect the detection and measurement of kilonovae and cut down the number of predicted detections. Even under ToO observations, it is necessary to choose the exposure time wisely to balance the coverage of sky area and detection depth, given the rapid evolution of kilonovae.

We also compute and simulate the situations of the other wide-field surveys which are dedicated to fast-transient discovery: LSST (LSST Science Collaboration et al. 2017; Ivezić et al. 2019) and ZTF (Bellm et al. 2019; Graham et al. 2019). The sky brightness of the sites and the other parameters of the telescopes used in simulation are shown in Table 1. The contrast of detection efficiency of these projects with WFST is presented in Figure 8 and their detection depths of 90% and 50% efficiency are also shown in Table 5. Because of the different FoVs of these telescopes, in order to reflect their detection abilities for AT2017gfo-like kilonovae reasonably, their exposure times need to be different according to their FoVs. Assuming the same total coverage of sky area and search time, the exposure time used is inversely proportional to the FoV size under full coverage. Hence, we set the exposure times as 30, 40, and 200 s for WFST, LSST, and ZTF, respectively. From Table 1 and Table 5, although the FoV of ZTF is much larger than that of WFST, for distant BNSs, WFST can perform better than ZTF and increase the search depth to 200–300 Mpc with 90% detection efficiency. By simulation in the Southern Hemisphere, LSST is expected to be more powerful and can reach $\sim$600 Mpc ($z = 0.13$) in searches for kilonovae. Our result is consistent with the detectability study presented by Scolnic et al. (2017), who predicted a detectable redshift range of $z = 0.02$–0.25 for LSST based on an AT2017gfo-like model. Given the geographical locations of WFST and LSST, WFST

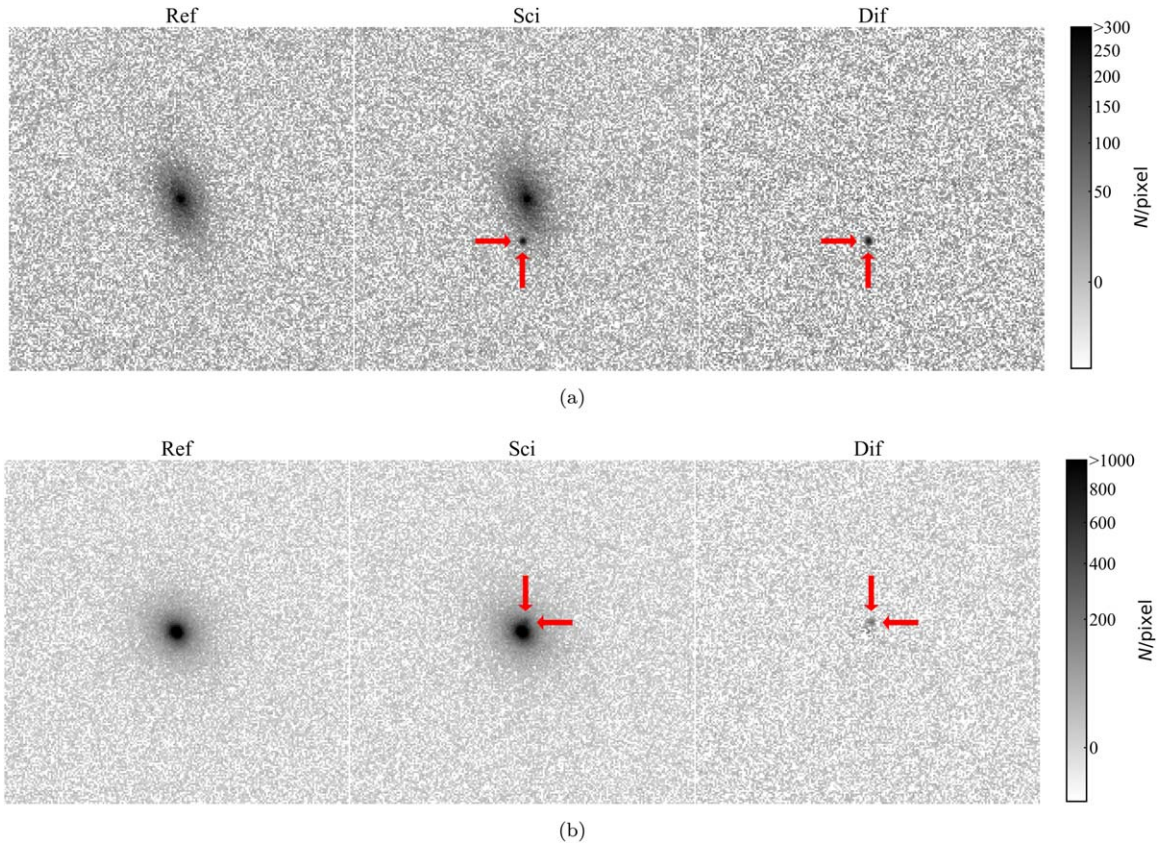

Figure 5. Example reference, science, and difference images with simulated host galaxies at redshift $z \sim 0.056$. (a) and (b) correspond to cases far from (with a physical offset of $r = 1.763$ kpc) and close to (with $r = 0.414$ kpc) the host galaxy's nucleus, respectively. The red arrows indicate the location of the kilonova.

can complement LSST for optical follow up in the Northern Hemisphere well to cover GW events across the entire sky.

To guide the selection of exposure time in searching for kilonovae, we also consider the rapid decay of kilonova luminosity. In the case of one or two magnitudes fainter than peak luminosity, which roughly corresponds to the 2nd and 3rd day after the merger (Kasliwal et al. 2020), their results are shown in Figure 9. When the luminosity decays by one magnitude from the peak, the detection depth with the same efficiency decreases a lot, which indicates that it is essential to make the best out of the hours around the peak and increase the exposure time in the following days after the peak.

4. ToO Optimization with WFST

In this section, based on the simulation, we investigate ToO observation optimization for WFST and discuss the follow-up ability and detection prospects with WFST for the upcoming O4.

4.1. Optimize the Exposure Time

After a GW alert triggers, brief information about the GW event is expected to be released by the Gamma-Ray Coordinates Network platform. Then, follow-up observations will begin based on the BAYESTAR sky map or the LALInference sky map, which include more detailed information about the location and distance. Due to the different methods used, the difference between these sky maps is the computing time and estimation accuracy, and the BAYESTAR sky maps are always released earlier but have worse estimations. By analyzing the `fits` file of the sky map, the probability distributions of the location and luminosity distance can be obtained and used for ToO observation design. Combining the luminosity distance from the GW alert and the ability of the telescope, we can choose an appropriate exposure time so that WFST can strike a balance between depth and coverage.

About the luminosity distance in the `fits` file of the sky map, detailed introductions are given in Singer et al. (2016a, 2016b). The sample of luminosity distance follows the distribution:

$$p(r|\boldsymbol{n}) = \frac{N(\boldsymbol{n})}{\sqrt{2\pi}\sigma(\boldsymbol{n})} \exp\left[-\frac{(r-\mu(\boldsymbol{n}))^2}{2\sigma(\boldsymbol{n})^2}\right] r^2 \quad \text{for } r \geqslant 0, \tag{4}$$

where $\boldsymbol{n}$ is a direction vector, which means the direction to a certain pixel of the sky based on the Hierarchical Equal Area isoLatitude Pixelisation (HEALPix) algorithm, and the parameters N, μ, and σ are stored in the `fits` file. We choose the distance $r_{\rm thred}$ with the 90% quantile of the distribution as the merger's location. By taking into account the result of the detection efficiency in Section 4, the exposure time is selected from an optional time list set as [30, 60, 90, 120, 180, 240, 300 s], and we require the efficiency is no less than 90% at $r_{\rm thred}$. If the maximum exposure in the list is insufficient to meet the threshold efficiency, the exposure time is set at 300 s. For the detection efficiency, there are three related parameters: exposure time, kilonova brightness, and bandpass. Given the

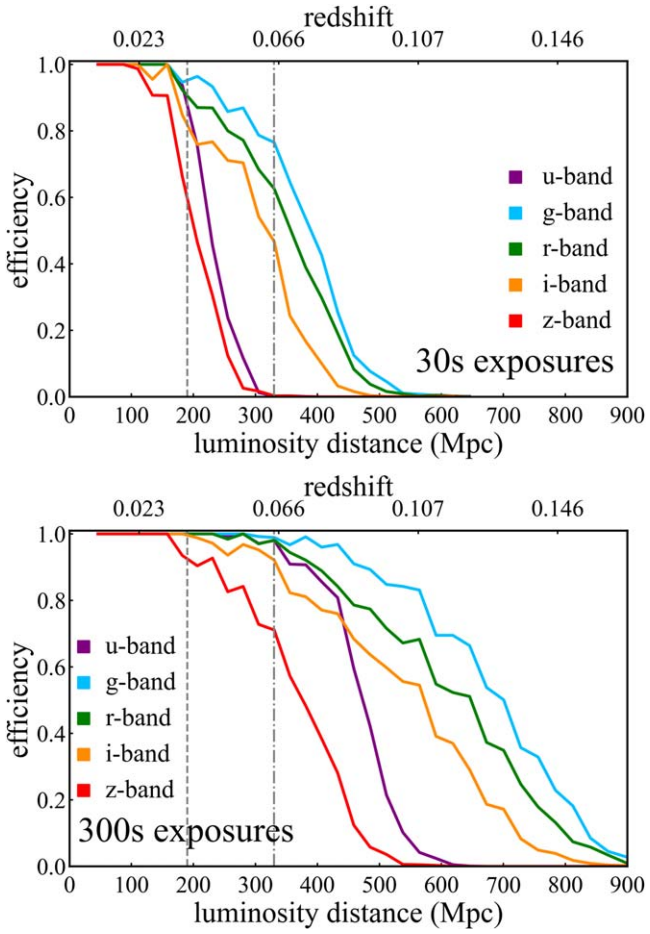

Figure 6. At peak of an AT2017gfo-like kilonova, the results of the detection efficiency varies with redshift for WFST with 30 (upper) and 300 s (lower) exposures. The gray dashed and dotted–dashed lines represent the detection range for BNSs during O4 and O5 (Abbott et al. 2020).

different exposure times for the telescope according to various events and observation nights.

4.2. Follow-up Ability and Prospects

Determining how much time is needed to cover the probable sky region in a follow-up observation can reflect the feasibility to search for kilonovae and guide us to allocate observation time for various GW events. However, in practice the total time of a follow-up observation is usually affected by too many factors, e.g., occurrence time, localization accuracy, weather, and Moon phase. To reflect the ability of WFST to conduct a follow-up search in O4, we investigate the average total time of ToO observations under various localization areas and distances.

The probable localization is assumed to be ideal enough, which means the observation is not influenced much by the Moon, the foreground of the Milky Way, and the weather. Combining the localization area of the event and the telescope's FoV, the number of images taken can be roughly estimated. By sampling the trigger time of GW events randomly in a day, based on the selection rule above, the exposure time for each observable time can be determined. We can subsequently match the exposure time to each pointing of the telescope and calculate the total time for covering the target sky. According to the prospects of the localization of GW events in Abbott et al. (2020), the median localization area of a BNS merger from LHVK measurements in O4 is 33^{+5}_{-5} deg^2. Since the localization accuracy is sensitive to the S/N of the signal and the number of detectors, the localization area with 90% confidence of most events might be hundreds to even thousands of square degrees in O4 (Petrov et al. 2022). Consequently, we set the calculation range of luminosity distance and localization area as 0–500 Mpc and 0–1250 deg^2, respectively.

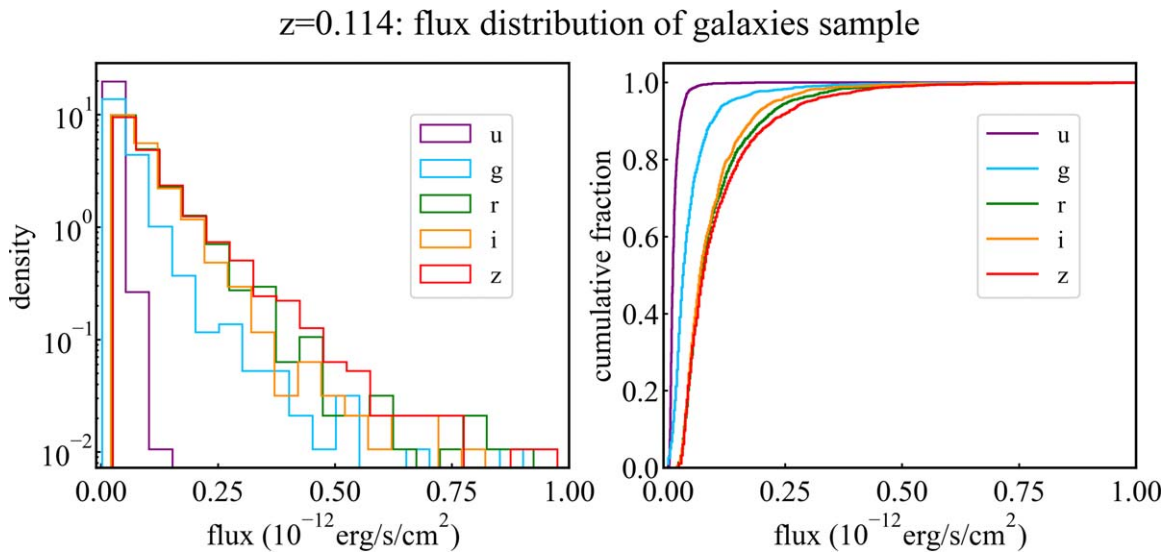

Figure 7. The flux distribution of the galaxy sample in CosmoDC2 for each band of WFST at redshift of $z = 0.114$.

occurrence time of the merger, we use interpolation to generate the detection efficiency curve under other exposure times and the average magnitude of each observable time which can be calculated using `Astropy`. Thus, we can reasonably set

The results of the total time with only one band and two bands are shown in Figure 10. To investigate the influence of the observable time per night of different seasons, we set two calculation dates to 2023 June 21 and 2023 December 23 to represent the cases of summer and winter. Comparing

Table 4
The Detection Depths with 90% and 50% Efficiency Calculated by Image Simulation of WFST with 30, 90, and 300 s Exposures

Exposure Time (s)	Efficiency	z_{max} ($D_{L,max}$ Mpc)				
		u	*g*	*r*	*i*	*z*
30	90%	0.039 (175.3)	0.055 (246.7)	0.046 (205.8)	0.038 (168.4)	0.036 (158.5)
	50%	0.051 (230.4)	0.084 (386.7)	0.078 (357.3)	0.069 (316.0)	0.045 (202.0)
90	90%	0.06 (270.2)	0.074 (336.8)	0.06 (271.9)	0.052 (235.5)	0.039 (172.0)
	50%	0.074 (340.0)	0.112 (525.3)	0.103 (479.1)	0.091 (422.7)	0.063 (286.8)
300	90%	0.084 (386.1)	0.104 (484.8)	0.086 (394.4)	0.072 (327.6)	0.05 (224.6)
	50%	0.102 (473.0)	0.145 (693.2)	0.133 (632.9)	0.12 (565.0)	0.082 (377.6)

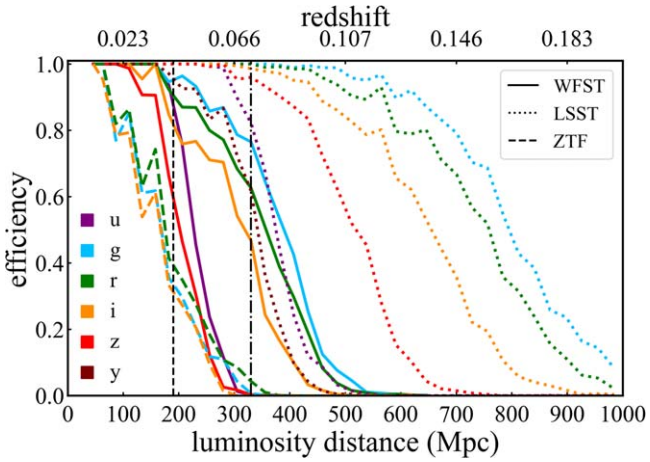

Figure 8. The result of detection efficiency varies with redshift for different telescopes at peak flux for a AT2017gfo-like kilonova. For comparing the search ability of kilonovae reasonably, the exposure time is set as 30, 40, and 200 s for WFST, LSST, and ZTF, respectively. The black dashed and dotted–dashed lines represent the detection range for BNSs during O4 and O5 (Abbott et al. 2020).

wavelengths in the telescope's optics, especially for the *u* and *g* bands of WFST. Referring to the GW ToO strategy of LSST (Andreoni et al. 2022), we choose the *g* and *r* bands in dark times of the Moon phase and a longer-wavelength band combination of the *r* and *i* bands in bright times, which correspond to Figures 10(c) and 10(d), respectively. The total time spent using the *r* and *i* bands is slightly longer than the *g* and *r* bands, which is predictable according to our optimization method of exposure time. Additionally, the limiting magnitude can also be reduced depending on the Moon phase as well as the angular distance between the pointing of the telescope and the Moon. Therefore, in practice appropriately avoiding the sky close to the Moon is necessary to ensure the overall efficiency. Assuming that the observation time per night is ∼4 hr, and it is more promising to find the kilonovae in the first two nights, we find WFST can search for kilonovae well if the localization area is no more than 10^3 deg^2, given the detection limit of GW detectors in O4. If the localization accuracy is poor ($>10^3$ deg^2), as reported for some events in O3, it is necessary to give up part of the area and focus on areas with relatively high probabilities. Based on this result, if the localization area

Table 5
The Detection Depths with 90% and 50% Efficiency Calculated by Image Simulation for WFST, LSST, and ZTF

Telescope	Efficiency	z_{max} ($D_{L,max}$ Mpc)					
		u	*g*	*r*	*i*	*z*	*y*
WFST	90%	0.039 (175.3)	0.055 (246.7)	0.046 (205.8)	0.038 (168.4)	0.036 (158.5)	⋯
	50%	0.051 (230.4)	0.084 (386.7)	0.078 (357.3)	0.069 (316.0)	0.045 (202.0)	
LSST	90%	0.067 (304.6)	0.131 (623.7)	0.113 (532.2)	0.098 (454.3)	0.084 (387.7)	0.054 (242.1)
	50%	0.082 (375.1)	0.165 (799.3)	0.156 (751.5)	0.137 (653.7)	0.11 (517.1)	0.074 (340.4)
ZTF	90%	⋯	0.018 (78.7)	0.019 (84.5)	0.016 (71.2)	⋯	⋯
	50%		0.037(165.3)	0.04(180.5)	0.036(159.0)		

Note. Exposure time is set as 30, 40, and 200 s for WFST, LSST, and ZTF, respectively.

Figures 10(a) and 10(b), there is not much difference in the total time between summer and winter at the Lenghu site, but the target sky can be covered earlier in winter due to there being more time available per night. To filter and confirm the kilonova candidate further, using at least two bands are necessary for getting a color evolution in actual observation. Therefore, the results of two-band coverage in summer are also calculated and shown in Figures 10(c) and 10(d). GW170817 and another possible BNS event, GW190425, reported during O3, are also marked in each panel. GW190425 is placed on the axes due to its bad localization. For the band choice, the combination between the *g* , *r*, and *i* bands are preferred for their relatively higher efficiency to search for kilonovae. In addition, a bright Moon phase can considerably affect shorter

of most BNS events detected in O4 is hundreds of square degrees, WFST can detect most kilonova counterparts of GW events. Assuming WFST can observe the sky where decl. $> -30°$, among kilonovae that are more than 15° from the disk of the Milky Way, only 57% events can be searched by WFST. Combined with the expected BNS detection of 10^{+53}_{-10} during O4 in Abbott et al. (2020) and the weather efficiency of 76% of the site (Deng et al. 2021), and roughly considering the influence of the Moon and the Sun, WFST is expected to find ∼30% (3^{+16}_{-3}) of kilonovae from BNS mergers during O4.

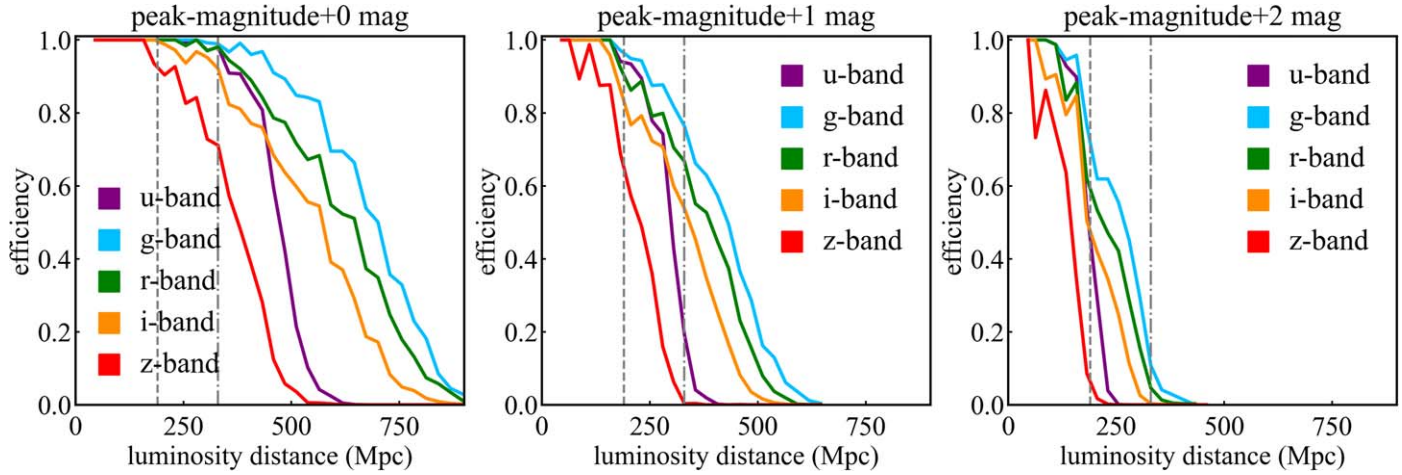

Figure 9. At different times of evolution of an AT2017gfo-like kilonova, the detection efficiency for WFST with 300 s exposures. The gray dashed and dotted–dashed lines represent the detection range for BNSs during O4 and O5 (Abbott et al. 2020).

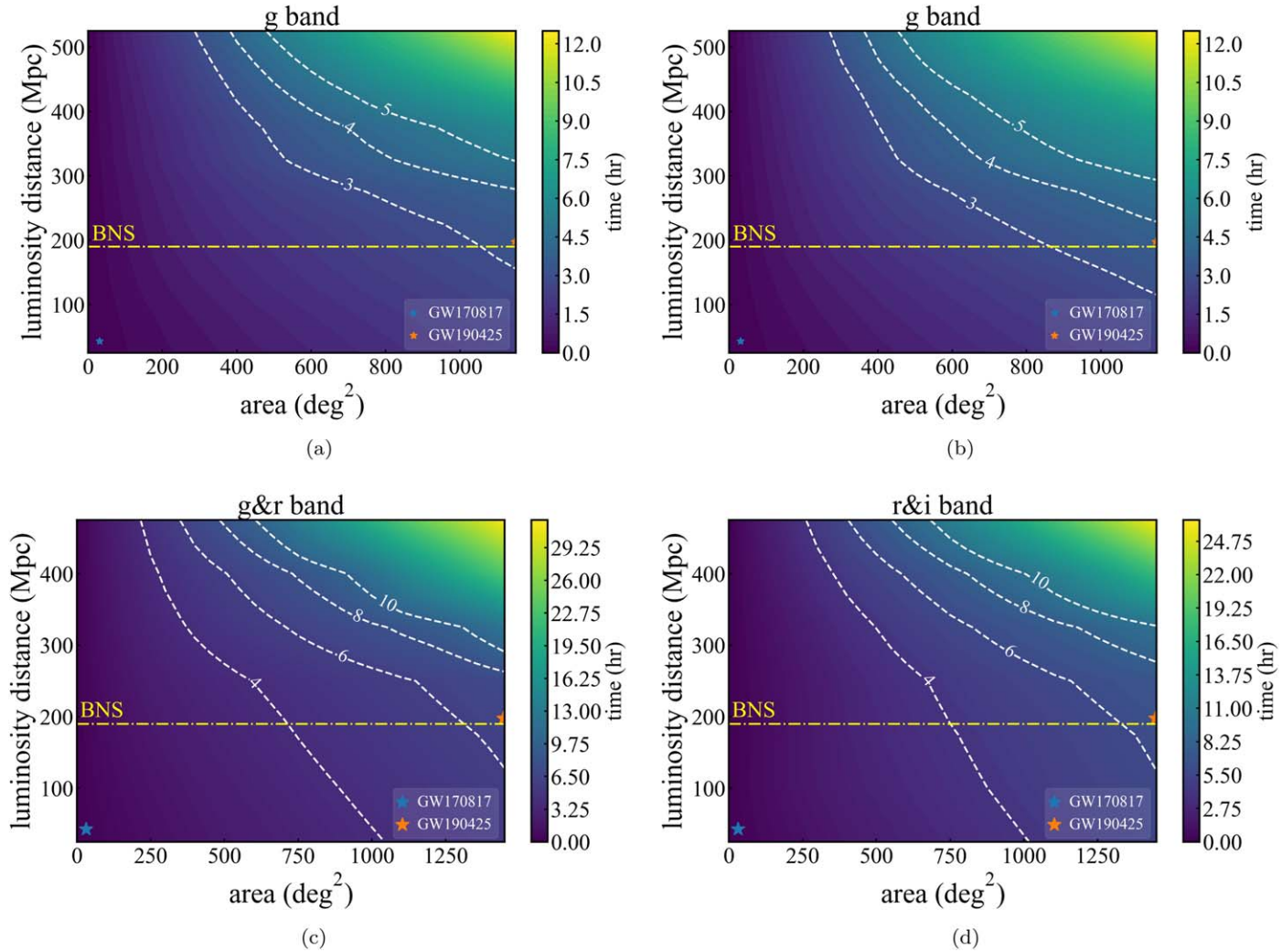

Figure 10. The results of the total time used in ToO observations with different localizations and luminosity distances. The dates of (a), (c), and (d) are set to 2023 June 21 and (b) is 2023 December 23. The dotted–dashed line annotates the limit distance for detecting a typical BNS merger in O4 (Abbott et al. 2020). White dashed lines represent contour lines of different times. GW170817 and another possible BNS event, GW190425, detected in O3, are also drawn in each panel, represented by star markers. Their distances are taken as $\mu + \sigma$, where μ and σ are the median and standard deviation, respectively, and the localization area is the part with 90% confidence where decl. $> -30°$. The event that is out of the calculation range is drawn on the axes.

5. Discussions and Conclusions

5.1. The Influence of Different Kilonova Models

The detection efficiency of the telescope depends on the kilonova model. However, the physical model of kilonovae is still unclear, even for a given BNS parameter, the viewing angle, and the equation of state of NSs. Since only one event, i.e., GW170817, is confirmed until now, various models are proposed in the literature, and most of them can explain the data fairly well (see for instance Metzger 2019; Nakar 2020; Margutti & Chornock 2021). In observations, there are six sGRBs with potential kilonova emission detected, with different levels of observational evidence. These sGRB kilonovae support the existence of a broad range of kilonova luminosities (∼0.3–10 times the luminosity of AT2017gfo depending on the epoch and frequency of observations; Ascenzi et al. 2019), which might hint at the diversity of kilonova models (Margutti & Chornock 2021). In the previous discussion, we ignored these model uncertainties, and simply assumed that all the events are AT2017gfo-like. In order to investigate the effects of different kilonova models on the detection efficiency, we simulate a sample of BNS models and consider the alternative kilonova model to calculate the luminosity of the events.

In fact, the luminosities of kilonovae can be different depending on the properties of the BNS systems. Based on the results of different kilonova luminosities in Figure 9, combined with a kilonova sample generated from various BNS systems, the detection efficiency can be estimated simply for kilonovae deviating from the AT2017gfo-like kilonovae. To construct a kilonova sample, we refer to the method in Wang et al. (2022) and introduce the method as follows.

To obtain the corresponding kilonova of each BNS system in the sample, we use the kilonova model (`bns` model) in Nicholl et al. (2021). Similar to the previous model used in this paper, the `bns` model is also composed of three-component ejecta matter which includes blue, purple, and red components. These components correspond to different generation mechanisms, because of which the opacity and atomic mass number of the diverse components are different. In contrast to the previous model, the geometry of the ejecta is axisymmetric in the `bns` model, where the blue and purple components mainly distribute around the pole direction and the red component concentrates around the equatorial plane, so the influence of the observer viewing angle on the light curves can be considered. Using the fitting results of the relativistic numerical calculations in Dietrich & Ujevic (2017), the authors connected the parameters of each ejecta matter component with the mass ratio and chirp mass of a BNS system. The mass and velocity of the ejecta matter can be calculated from the masses of BNSs. In addition, the other two effects that can contribute additional luminosity to kilonovae are also considered: (1) an enhancement in the blue ejecta due to magnetically driven winds and (2) the shock heating of the ejecta by a GRB jet, where (1) can be possible only if the remnant avoids prompt collapse (Metzger et al. 2018), and (2) can contribute to the blue luminosity during the early evolution of kilonovae (Arcavi 2018).

The free parameters of the `bns` model fitting AT2017gfo are the mass ratio (q), chirp mass ($\mathcal{M}$), symmetric tidal deformability (Λ_s), redshift (z), observer viewing angle (θ), enhancement factor of blue ejecta by surface winds (α), fraction of disk ejected ($\epsilon_{\rm disk}$), maximum stable NS mass ($M_{\rm TOV}$), and opening angle of the shocked cocoon ($\theta_{\rm c}$). The mass ratio and the chirp mass can be derived from the NS mass by the following equations:

$$q = \frac{M_1}{M_2} \leqslant 1, \tag{5}$$

$$\mathcal{M} = \frac{(M_1 M_2)^{3/5}}{(M_1 + M_2)^{1/5}}. \tag{6}$$

The observer viewing angle of each BNS is sampled uniformly from $\pi/2$ to $-\pi/2$. To compare these light curves with AT2017gfo directly, the redshift is set as $z = 0.0098$, which is the same as AT2017gfo (Soares-Santos et al. 2017). The symmetric tidal deformability can be calculated from q and $\mathcal{M}$. The symmetric tidal deformability Λ_s and the antisymmetric tidal deformability Λ_s are defined as $\Lambda_s \equiv \Lambda_1 + \Lambda_2$ and $\Lambda_a \equiv \Lambda_1 - \Lambda_2$, respectively, where Λ_1 and Λ_2 are the external tidal fields of the BNS. The relationship between Λ_s and Λ_a is given in Yagi & Yunes (2016):

$$\Lambda_a = F_{\bar{n}}(q)\Lambda_s \frac{a + \sum_{i=1}^{3}\sum_{j=1}^{2} b_{ij} q^j \Lambda_s^{-i/5}}{a + \sum_{i=1}^{3}\sum_{j=1}^{2} c_{ij} q^j \Lambda_s^{-i/5}}, \tag{7}$$

$$F_n(q) \equiv \frac{1 - q^{10/(3-n)}}{1 + q^{10/(3-n)}}, \tag{8}$$

where $a = 0.0755$ and $\bar{n} = 0.743$, which means the average factor of various equations of state, and b_{ij} and c_{ij} are listed in Table 6. A specific combination of Λ_1 and Λ_2 can be constrained by GW information (Wade et al. 2014; Favata 2014):

$$\tilde{\Lambda} = \frac{16}{13}\frac{(12q + 1)\Lambda_1 + (12 + q)q^4\Lambda_2}{(1 + q)^5}, \tag{9}$$

called the binary or effective tidal deformability, which can also be calculated according to the empirical relationship with the radius of a $1.4\,M_\odot$ NS ($R_{1.4}$):

$$\tilde{\Lambda} \simeq 800\left(\frac{R_{1.4}}{11.2}\frac{M_\odot}{\mathcal{M}}\right)^6. \tag{10}$$

Based on a certain $R_{1.4}$ and $M_{\rm TOV}$, Λ_s can be calculated using Equations (7), (8), (9), and (10). The undetermined parameters are set referring to the best-fitting result of AT2017gfo in Nicholl et al. (2021) as $\epsilon_{\rm disk} = 0.12$, $\alpha = 0.63$, $M_{\rm TOV} = 2.17\,M_\odot$, $R_{1.4} = 11.06$ km, and $\cos\theta_{\rm c} = 0.91$.

We refer to the results in Farrow et al. (2019) to construct the BNS sample. In the standard isolated binary formation channel, a recycled NS is born first and spins up to ∼10–100 ms by an accretion/recycling process. Its companion, a nonrecycled NS, quickly spins down to an $\mathcal{O}(1)$ s period after birth (Tauris et al. 2017). By fitting 17 Galactic BNS systems, in the best-fitting case, Farrow et al. (2019) found that the nonrecycled NS masses are distributed uniformly, and the recycled NS masses

Table 6
The Value of the Parameters Used in Equation (7)

b_{ij}	$i=1$	$i=2$	$i=3$	c_{ij}	$i=1$	$i=2$	$i=3$
$j=1$	−2.235	10.45	−15.75	$j=1$	−2.048	7.941	−7.36
$j=2$	0.847	−3.25	13.61	$j=2$	0.598	0566	−1.32

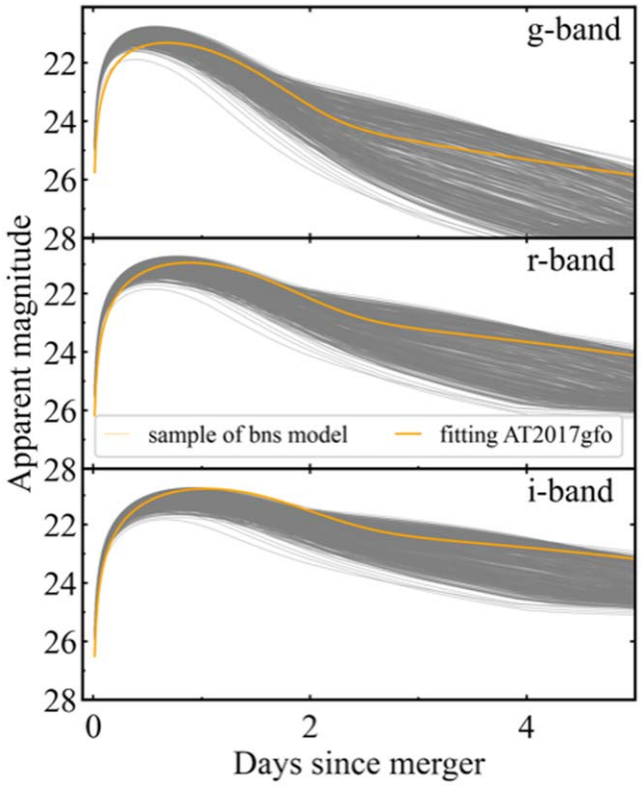

Figure 11. The light curves calculated from `bns` model (gray) and fitting AT2017gfo light curves (orange) in the *g*, *r*, and *i* bands of WFST. Their redshifts are set as the same with AT2017gfo.

distribute according to a two-Gaussian distribution:

$$\pi(m|\mu_1, \sigma_1, \mu_2, \sigma_2, \alpha) = \frac{\alpha}{\sigma_1\sqrt{2\pi}} \times \exp\left[-\left(\frac{m-\mu_1}{\sqrt{2}\,\sigma_1}\right)^2\right] + \frac{1-\alpha}{\sigma_2\sqrt{2\pi}}\exp\left[-\left(\frac{m-\mu_2}{\sqrt{2}\,\sigma_2}\right)^2\right], \quad (11)$$

where the fitting parameters are $\mu_1 = 1.34\,M_\odot$, $\mu_2 = 1.47\,M_\odot$, $\sigma_1 = 0.02\,M_\odot$, $\sigma_2 = 0.15\,M_\odot$, and $\alpha = 0.68\,M_\odot$. For the non-recycled NS, the range of uniform mass distribution is 1.16–1.42 $M_\odot$. According to this fitting result, the NS masses of the BNS systems can be sampled.

Combined with the BNS sample and `bns` model, in the *g*, *r*, and *i* bands of WFST, the light curves of a sample of 500 BNS systems are calculated and shown in Figure 11 as a cluster of gray lines. As contrast, the light curves of fitting AT2017gfo-like kilonova are also drawn as orange lines. From Figure 11, the evolution of AT2017gfo can be included well in our sample. Compared with the AT2017gfo, a kilonova in the sample has a lower luminosity than AT2017gfo in most cases, which is broadly consistent with the result in Chase et al. (2022), where the authors generated a kilonova sample based on another model (SuperNu) to investigate kilonova detectability. In Figure 3 of Chase et al. (2022), in the *r* band of LSST, the detection depth of AT2017gfo is farther away than most of the sample, which means that AT2017gfo is more luminous in the sample. In the first two days, which is the most promising time to detect the kilonova, the magnitude difference between the kilonovae sample and AT2017gfo is −0.5–1 mag. For an extreme case that a kilonova is 1 mag fainter than AT2017gfo at peak luminosity, the detection depths (observed by WFST with 90% efficiency and a 300 s exposure time) decrease to ∼200 Mpc according to Figure 9. Therefore, considering the luminosity function of kilonovae, the average predicted detection range can further decrease compared to the AT2017gfo-like kilonovae.

5.2. Conclusion

This work explores the impact of image subtraction and host galaxy interference on WFST's ability to detect kilonovae and uses these results to optimize the exposure selection for future ToO observations. Based on python packages of `GalSim` and `PythonPhot`, considering an AT2017gfo-like kilonova fitted and generated by `MOSFiT`, we generate simulated reference and science images and test this process with a flat background. We find that under the dark night-sky background of the site in Table 1, the detection depths considering image subtraction are shallower than those calculated by comparing the kilonova magnitude with the limiting magnitude of the telescope. Given the spectrum of an AT2017gfo-like kilonova, the *g* and *r* bands are more effective in searching for kilonovae, which is consistent with the results in Zhu et al. (2023) and Chase et al. (2022). If the kilonova is not detected around peak, the longer-wavelength bands can be useful to keep searching according to the spectral evolution of kilonovae (Kasen et al. 2017).

Based on the flat background simulation, we add host galaxies from the synthetic catalog CosmoDC2 into the images to explore the effects of the hosts. Using the stellar mass as an indicator to quantify the BNS merger rate of the galaxy, we filter out galaxies which are less likely to be a host. The distance from the galaxy center is sampled following the offset distribution observed for sGRBs. We obtained the detectability at different redshifts and find that although the BNS mergers are farther away from the host centers compared with SNe and TDEs, the host backgrounds can significantly affect kilonova detection and cannot be ignored. After taking into account the host galaxy, for the peak of an AT2017gfo-like kilonova, the detection depth reduces from 357 (338) Mpc to 246 (213) Mpc in the *g* (*r*) band. The detection at longer wavelengths is affected more severely by the presence of a host galaxy, because of the spectral shape of BNS hosts. Given these influences, a longer exposure time is recommended in ToO follow up.

We also compare the detection efficiency of WFST, LSST, and ZTF, and their exposure times are inversely proportional to their FoVs. With 90% detection efficiency, LSST proves to be the most efficient and can reach ∼500 Mpc with 40 s exposures. Although the FoV of ZTF is much larger than that of WFST, with a deeper detection depth, WFST can do better than ZTF for distant kilonovae. For the upcoming O4 and O5, WFST can coordinate with LSST appropriately to cover the probable region in the Northern Hemisphere. As the kilonova evolves and becomes dim after the peak, the detection depth of WFST decreases drastically, therefore the effective observation window is within the first two nights. To estimate how realistic is the choice of AT2017gfo as a template, we construct a kilonova sample based on the `bns` model and the fitting mass distributions of BNSs. AT2017gfo belongs to the more luminous case in the sample, and the magnitude difference between the sample and AT2017gfo is −0.5–1 mag, which

means that the detection range can further decrease considering the kilonova diversity.

According to the detectability results above, we optimize the exposure time for every night and estimate the average total time to cover a region of GW localization in a ToO observation. Considering two nights and four hours each night to observe, with two bands WFST can well deal with the case that the localization region is no more than $\sim$1000 deg^2 at 300 Mpc. Based on the simulation of BNS detection in O4 (Abbott et al. 2020), WFST can search and find most kilonovae if the probable sky region is observable and is predicted to find $\sim$30% of the kilonovae of BNS mergers reported in O4.

We note that in O3 ZTF applied package `gwemopt` to design and generate observation sequences (Coughlin et al. 2018; Almualla et al. 2020). A similar package can be used for WFST to increase the observation efficiency combined with the chosen exposure method in this work.

We appreciate the helpful discussions in the WFST science team. This work is supported by the National Key R&D Program of China grant Nos. 2021YFC2203102 and 2022YFC2200100, NSFC No. 12273035, the Fundamental Research Funds for the Central Universities under Grant Nos. WK2030000036 and WK3440000004, and Cyrus Chun Ying Tang Foundations.

Facility: WFST.

Software: `MOSFiT` (Villar et al. 2017; Guillochon et al. 2018), `GalSim` (Rowe et al. 2015), `PythonPhot` (Jones et al. 2015), `NumPy` (van der Walt et al. 2011; Harris et al. 2020), `Astropy` (Robitaille et al. 2013), `SciPy` (Virtanen et al. 2020), `matplotlib` (Hunter 2007).

ORCID iDs

Zheng-Yan Liu https://orcid.org/0000-0002-2242-1514
Zhe-Yu Lin https://orcid.org/0000-0003-4959-1625
Ji-Ming Yu https://orcid.org/0000-0001-6319-0866
Hui-Yu Wang https://orcid.org/0000-0001-7081-8623
Wen Zhao https://orcid.org/0000-0002-1330-2329
Zi-Gao Dai https://orcid.org/0000-0002-7835-8585

References

Abbott, B. P., Abbott, R., Abbott, T. D., et al. 2017, PhRvL, 119, 161101
Abbott, B. P., Abbott, R., Abbott, T. D., et al. 2020, LRR, 23, 3
Ackley, K., Amati, L., Barbieri, C., et al. 2020, A&A, 643, A113
Almualla, M., Coughlin, M. W., Anand, S., et al. 2020, MNRAS, 495, 4366
Anand, S., Coughlin, M. W., Kasliwal, M. M., et al. 2021, NatAs, 5, 46
Andreoni, I., Goldstein, D. A., Anand, S., et al. 2019, ApJL, 881, L16
Andreoni, I., Goldstein, D. A., Kasliwal, M. M., et al. 2020, ApJ, 890, 131
Andreoni, I., Margutti, R., Salafia, O. S., et al. 2022, ApJS, 260, 18
Arcavi, I. 2018, ApJL, 855, L23
Arcavi, I., Hosseinzadeh, G., Howell, D. A., et al. 2017, Natur, 551, 64
Artale, M. C., Mapelli, M., Bouffanais, Y., et al. 2020, MNRAS, 491, 3419
Artale, M. C., Mapelli, M., Giacobbo, N., et al. 2019, MNRAS, 487, 1675
Ascenzi, S., Coughlin, M. W., Dietrich, T., et al. 2019, MNRAS, 486, 672
Belczynski, K., Bulik, T., & Kalogera, V. 2002, ApJ, 571, L147
Belczynski, K., Perna, R., Bulik, T., et al. 2006, ApJ, 648, 1110
Bellm, E. C., Kulkarni, S. R., Graham, M. J., et al. 2019, PASP, 131, 018002
Blanchard, P. K., Berger, E., Fong, W., et al. 2017, ApJL, 848, L22
Bloom, J. S., Sigurdsson, S., & Pols, O. R. 1999, MNRAS, 305, 763
Bulla, M. 2019, MNRAS, 489, 5037
Cao, L., Lu, Y., & Zhao, Y. 2018, MNRAS, 474, 4997
Chase, E. A., O'Connor, B., Fryer, C. L., et al. 2022, ApJ, 927, 163
Coughlin, M. W., Tao, D., Chan, M. L., et al. 2018, MNRAS, 478, 692
Coulter, D. A., Foley, R. J., Kilpatrick, C. D., et al. 2017, Sci, 358, 1556
Cowperthwaite, P. S., Villar, V. A., Scolnic, D. M., & Berger, E. 2019, ApJ, 874, 88
Cowperthwaite, P. S., & Berger, E. 2015, ApJ, 814, 25
Cowperthwaite, P. S., Berger, E., Villar, V. A., et al. 2017, ApJL, 848, L17
Dálya, G., Díaz, R., Bouchet, F. R., et al. 2022, MNRAS, 514, 1403
Dálya, G., Galgóczi, G., Dobos, L., et al. 2018, MNRAS, 479, 2374
Deng, L., Yang, F., Chen, X., et al. 2021, Natur, 596, 353
Dietrich, T., & Ujevic, M. 2017, CQGra, 34, 105014
Eichler, D., Livio, M., Piran, T., & Schramm, D. N. 1989, Natur, 340, 126
Evans, P. A., Cenko, S. B., Kennea, J. A., et al. 2017, Sci, 358, 1565
Farrow, N., Zhu, X.-J., & Thrane, E. 2019, ApJ, 876, 18
Favata, M. 2014, PhRvL, 112, 101101
Flaugher, B., Diehl, H. T., Honscheid, K., et al. 2015, AJ, 150, 150
Fong, W., & Berger, E. 2013, ApJ, 776, 18
Fong, W., Berger, E., & Fox, D. B. 2010, ApJ, 708, 9
Fong, W., Berger, E., Margutti, R., & Zauderer, B. A. 2015, ApJ, 815, 102
Fong, W., Laskar, T., Rastinejad, J., et al. 2021, ApJ, 906, 127
Fong, W., Margutti, R., Chornock, R., et al. 2016, ApJ, 833, 151
Giacobbo, N., & Mapelli, M. 2018, MNRAS, 480, 2011
Goldstein, A., Veres, P., Burns, E., et al. 2017, ApJL, 848, L14
Graham, M. J., Kulkarni, S. R., Bellm, E. C., et al. 2019, PASP, 131, 078001
Guillochon, J., Nicholl, M., Villar, V. A., et al. 2018, ApJS, 236, 6
Harris, C. R., Millman, K. J., Van Der Walt, S. J., et al. 2020, Natur, 585, 357
Hinshaw, G., Larson, D., Komatsu, E., et al. 2013, ApJS, 208, 19
Hotokezaka, K., & Nakar, E. 2020, ApJ, 891, 152
Hunter, J. D. 2007, CSE, 9, 90
Ivezić, Ž., Kahn, S. M., Tyson, J. A., et al. 2019, ApJ, 873, 111
Ivezić, Ž., Jones, R. L., & Lupton, R. 2010, The LSST Photon Rates and SNRCalculations, v1.2, http://faculty.washington.edu/ivezic/Teaching/Astr511/LSST_SNRdoc.pdf
Jin, Z.-P., Covino, S., Liao, N.-H., et al. 2020, NatAs, 4, 77
Jones, D. O., Scolnic, D. M., & Rodney, S. A. 2015, PythonPhot: Simple DAOPHOT-type photometry in Python, Astrophysics Source Code Library, ascl:1501.010
Kasen, D., Metzger, B., Barnes, J., Quataert, E., & Ramirez-Ruiz, E. 2017, Natur, 551, 80
Kasliwal, M. M., Anand, S., Ahumada, T., et al. 2020, ApJ, 905, 145
Kasliwal, M. M., Nakar, E., Singer, L. P., et al. 2017, Sci, 358, 1559
Korytov, D., Hearin, A., Kovacs, E., et al. 2019, ApJS, 245, 26
Lamb, G. P., Tanvir, N. R., Levan, A. J., et al. 2019, ApJ, 883, 48
Lamberts, A., Garrison-Kimmel, S., Hopkins, P. F., et al. 2018, MNRAS, 480, 2704
Landsman, W. B. 1993, in ASP. Conf Ser. 52, Astronomical Data Analysis Software and Systems II, ed. R. J. Hanisch, R. J. V. Brissenden, & J. Barnes (San Francisco, CA: ASP), 246
Lattimer, J. M., Mackie, F., Ravenhall, D. G., & Schramm, D. N. 1977, ApJ, 213, 225
Lattimer, J. M., & Schramm, D. N. 1974, ApJL, 192, L145
Lei, L., Zhu, Q.-F., Kong, X., et al. 2023, RAA, 23, 035013
Li, L.-X., & Paczyński, B. 1998, ApJ, 507, L59
Lin, Z., Jiang, N., & Kong, X. 2022, MNRAS, 513, 2422
LSST Science Collaboration, Marshall, P., Anguita, T., et al. 2017, arXiv:1708.04058
Mapelli, M., & Giacobbo, N. 2018, MNRAS, 479, 4391
Mapelli, M., Giacobbo, N., Toffano, M., et al. 2018, MNRAS, 481, 5324
Margutti, R., & Chornock, R. 2021, ARA&A, 59, 155
Metzger, B. D. 2019, LRR, 23, 1
Metzger, B. D., & Berger, E. 2012, ApJ, 746, 48
Metzger, B. D., Martínez-Pinedo, G., Darbha, S., et al. 2010, MNRAS, 406, 2650
Metzger, B. D., Thompson, T. A., & Quataert, E. 2018, ApJ, 856, 101
Nakar, E. 2020, PhR, 886, 1
Narayan, R., Paczynski, B., & Piran, T. 1992, ApJL, 395, L83
Nicholl, M., Margalit, B., Schmidt, P., et al. 2021, MNRAS, 505, 3016
O'Shaughnessy, R., Bellovary, J. M., Brooks, A., et al. 2017, MNRAS, 464, 2831
P200 2007, Sensitivities & sky brightness of Palomar observatory, https://sites.astro.caltech.edu/palomar/observer/200inchResources/sensitivities.html
Paczynski, B. 1986, ApJL, 308, L43
Paterson, K., Fong, W., Nugent, A., et al. 2020, ApJL, 898, L32
Petrov, P., Singer, L. P., Coughlin, M. W., et al. 2022, ApJ, 924, 54
Pian, E., D'Avanzo, P., Benetti, S., et al. 2017, Natur, 551, 67
Popham, R., Woosley, S. E., & Fryer, C. 1999, ApJ, 518, 356
Robitaille, T. P., Tollerud, E. J., Greenfield, P., et al. 2013, A&A, 558, A33
Rowe, B. T. P., Jarvis, M., Mandelbaum, R., et al. 2015, A&C, 10, 121
Savchenko, V., Ferrigno, C., Kuulkers, E., et al. 2017, ApJL, 848, L15
Scolnic, D., Kessler, R., Brout, D., et al. 2017, ApJL, 852, L3

Seabold, S., & Perktold, J. 2010, in 9th Python in Science Conference
Shappee, B. J., Simon, J. D., Drout, M. R., et al. 2017, Sci, 358, 1574
Singer, L. P., Chen, H.-Y., Holz, D. E., et al. 2016a, ApJL, 829, L15
Singer, L. P., Chen, H.-Y., Holz, D. E., et al. 2016b, ApJS, 226, 10
Smartt, S. J., Chen, T.-W., Jerkstrand, A., et al. 2017, Natur, 551, 75
Soares-Santos, M., Holz, D. E., Annis, J., et al. 2017, ApJL, 848, L16
Tanvir, N. R., Levan, A. J., Fruchter, A. S., et al. 2013, Natur, 500, 547
Tanvir, N. R., Levan, A. J., González-Fernández, C., et al. 2017, ApJL, 848, L27
Tauris, T. M., Kramer, M., Freire, P. C. C., et al. 2017, ApJ, 846, 170
Toffano, M., Mapelli, M., Giacobbo, N., Artale, M. C., & Ghirlanda, G. 2019, MNRAS, 489, 4622
Troja, E., Castro-Tirado, A. J., Becerra González, J., et al. 2019, MNRAS, 489, 2104
Tucker, D. L., Wiesner, M. P., Allam, S. S., et al. 2022, ApJ, 929, 115
van der Walt, S., Colbert, S. C., & Varoquaux, G. 2011, CSE, 13, 22
Villar, V. A., Guillochon, J., Berger, E., et al. 2017, ApJL, 851, L21
Virtanen, P., Gommers, R., Oliphant, T. E., et al. 2020, NatMe, 17, 261
Voss, R., & Tauris, T. M. 2003, MNRAS, 342, 1169
Wade, L., Creighton, J. D. E., Ochsner, E., et al. 2014, PhRvD, 89, 103012
Wang, F. Y., Wang, Y. Y., Yang, Y.-P., et al. 2020, ApJ, 891, 72
Wang, H., Yu, J., Liu, Z., Zhao, W., & Lu, Y. 2022, SCPMA, 50, 22
White, D. J., Daw, E. J., & Dhillon, V. S. 2011, CQGra, 28, 085016
Wollaeger, R. T., Fryer, C. L., Chase, E. A., et al. 2021, ApJ, 918, 10
Yagi, K., & Yunes, N. 2016, CQGra, 33, 13LT01
Yu, Y.-W., Liu, L.-D., & Dai, Z.-G. 2018, ApJ, 861, 114
Zhu, J.-P., Wu, S., Yang, Y.-P., et al. 2023, ApJ, 942, 88